



# Theoretical infrared signature of OH defects in Fe<sup>3+</sup>, Cr<sup>3+</sup> and Al<sup>3+</sup>-doped enstatite

Etienne Balan<sup>1</sup> · Jannick Ingrin<sup>2</sup>

Received: 27 May 2024 / Accepted: 29 June 2024 / Published online: 20 July 2024  
© The Author(s), under exclusive licence to Springer-Verlag GmbH Germany, part of Springer Nature 2024

## Abstract

The infrared spectroscopic properties of selected defects involving one proton and one nearby M<sup>3+</sup> (M = Al, Cr, Fe) substitution in orthoenstatite are investigated by first-principles calculations. Based on the theoretical results, the absorption bands experimentally observed on synthetic samples with high crystalline quality and low doping levels can be assigned to specific defect configurations. Most of them correspond to Mg vacancies at M2 sites locally compensated by one proton and one M<sup>3+</sup> cation at a nearby M1 site. This confirms that the M<sup>3+</sup> + H<sup>+</sup> = 2 Mg<sup>2+</sup> exchange mechanism is the dominant hydrogen incorporation mechanism at the lowest concentration levels in doped enstatite. At higher concentration levels, more complex incorporation mechanisms could become dominant in Al-bearing samples.

**Keywords** Enstatite · FTIR spectroscopy · OH defects · Ab initio modeling

## Introduction

Enstatite (Mg<sub>2</sub>(Si<sub>2</sub>O<sub>6</sub>)) is a major phase of the Earth's upper mantle that is known to incorporate various amounts of OH-bearing defects (Beran and Zemann 1986; Ingrin and Skogby 2000; Stalder and Skogby 2002; Rauch and Keppler 2002). Although these defects have been extensively studied by infrared spectroscopy and, more recently, by nuclear magnetic resonance (Xue et al. 2024), the corresponding atomic-scale geometries are still debated.

The OH-stretching spectrum of synthetic orthoenstatite usually displays two bands assigned to doubly protonated M2 vacancies. They are observed at 3070 and 3360 cm<sup>-1</sup> with maximum absorbance for a polarization parallel to [001] and almost no absorbance along [100] (Mierdel and Keppler 2004; Prechtel and Stalder 2010). Additional bands dominantly polarized along [100] are observed at 3592 and 3687 cm<sup>-1</sup> in samples synthesized at lower silica activity

and higher pressure (Prechtel and Stalder 2010, 2011). These two bands are most likely related to protons ensuring the charge compensation of Si<sup>4+</sup> vacancies (Balan et al. 2013; Xue et al. 2024). Assignment to a fourfold protonated vacancy ("hydrogarnet" defect, Xue et al. 2024) versus a partially protonated vacancy (Balan et al. 2013) remains an open question due to the lack of experimental evidence for the presence of strong OH bands below 3000 cm<sup>-1</sup> (see, e.g., Stalder et al. 2012).

In natural samples, OH-defects are expected to interact with various impurities, such as aluminum and other trivalent cations. These interactions can lead to rather complex infrared spectra with broadened absorption bands (e.g., Stalder et al. 2015). In comparison, synthetic enstatite samples with low concentration levels of trivalent impurities display narrow bands not observed in the pure Mg–Si–O–H system (Stalder 2004). Three bands are observed at 3283, 3322 and 3449 cm<sup>-1</sup> in Cr-doped samples, while only two bands are observed at 3328 and 3461 cm<sup>-1</sup> in Fe-doped samples (Fig. 1). Five major bands are observed at 3320, 3381, 3475, 3517 and 3548 cm<sup>-1</sup> in enstatite doped with 0.25 wt.% Al<sub>2</sub>O<sub>3</sub> (Fig. 1). They are also consistently reported for the Al-doped samples investigated by Stalder and Skogby (2002). All these bands are specifically related to the trivalent impurities and have a dominant polarization parallel to [001] (Stalder 2004), suggesting that they involve M vacancies.

✉ Etienne Balan  
Etienne.Balan@sorbonne-universite.fr

<sup>1</sup> Sorbonne Université, CNRS, MNHN, Institut de Minéralogie, de Physique Des Matériaux Et de Cosmochimie (IMPMC), 4 Place Jussieu, 75252 Paris cedex 05, France

<sup>2</sup> Univ. Lille, CNRS, INRAE, Centrale Lille, UMR 8207, UMET, Unité Matériaux Et Transformations, 59000 Lille, France

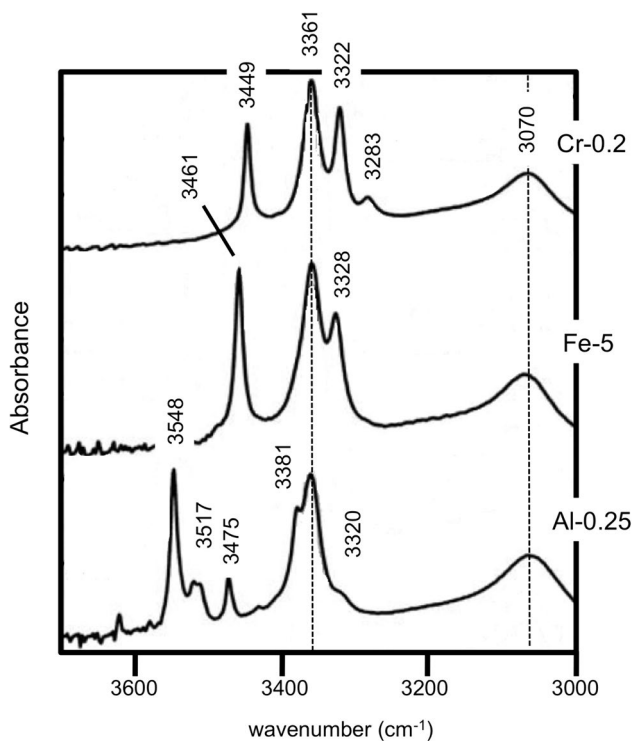


**Fig. 1** Experimental IR-spectra of synthetic orthopyroxenes doped with Cr, Fe and Al from Stalder (2004). The dotted lines correspond to the bands related to doubly protonated M2 vacancies, which are also observed in pure enstatite

In the present study, we theoretically determine the atomic-scale geometry and infrared spectroscopic properties of OH-bearing defects associated with major trivalent impurities in enstatite. The high crystalline quality and chemically well-constrained character of the samples synthesized and investigated by Stalder (2004) facilitate the comparison of experimental observations with the theoretical properties of OH-bearing defects. The results confirm that most of the bands observed by Stalder (2004) correspond to protonated M2 vacancies associated with trivalent cations and support their one-to-one assignment to a specific defect geometry.

## Theoretical modeling of OH-defects

The properties of OH-defects were theoretically investigated within the density functional theory (DFT) framework using the PWscf code of the Quantum Espresso package (Giannozzi et al. 2009; <http://www.quantum-espresso.org>). The modeling scheme used the generalized gradient approximation (GGA) to the exchange–correlation functional as proposed by Perdew, Burke and Ernzerhof (PBE functional; Perdew et al. 1996), and periodic boundary conditions. The ionic cores were described using optimized norm-conserving Vanderbilt (ONCV) pseudopotentials (Hamann 2013;

Schlipf and Gygi 2015) with a 80 Ry cut-off on the electronic wave functions. Unit-cell parameters of pure enstatite (space group *Pbca*) were optimized at zero pressure, using a shifted Monkhorst–Pack  $2 \times 2 \times 2$  k-point grid for the electronic integration. The theoretical cell parameters ( $a = 18.43$  Å,  $b = 8.92$  Å,  $c = 5.24$  Å) overestimate their experimental counterparts ( $a = 18.21$  Å,  $b = 8.81$  Å,  $c = 5.18$  Å; Morimoto and Koto 1969) as usually observed in GGA calculations. The vibrational properties of OH-bearing defects were determined using  $1 \times 2 \times 3$  supercells (480 atoms) containing one to two hydrogen atoms equivalent to a hydrogen concentration of 0.093 wt.% H<sub>2</sub>O and 0.187 wt.% H<sub>2</sub>O, respectively. These relatively large supercells help minimizing the interaction of the defects with their periodic images. The theoretical unit-cell parameters of pure enstatite were used without further relaxation to produce the supercells and the electronic integration was restricted to the  $\Gamma$  point. For all systems, the relaxation of atomic internal coordinates was performed until the residual forces were  $< 10^{-4}$  Ry/a.u.. For models containing isolated paramagnetic cations (Cr<sup>3+</sup>, Fe<sup>3+</sup>), spin-polarized calculations have been performed, imposing the high-spin state of the ion to the supercell.

The vibrational modes were calculated at the Brillouin zone center ( $\Gamma$  point), using the linear response theory (Baroni et al. 2001) as implemented in the PHonon code (Giannozzi et al. 2009; <http://www.quantum-espresso.org>). The high-frequency OH stretching modes that are decoupled from the other vibrational modes occurring at significantly lower frequency were calculated on the  $1 \times 2 \times 3$  supercell models by only considering the displacement of the oxygen and hydrogen atoms involved in the OH groups (Balan et al. 2008; Fuchs et al. 2022). The Born effective charge tensors and electronic dielectric tensor were obtained on the equivalent models computed with a smaller  $1 \times 1 \times 2$  supercell. The complex low-frequency dielectric permittivity tensor was calculated for each defect by adding only the ionic contributions related to the OH-stretching modes to the electronic permittivity tensor and using an arbitrary damping parameter of  $4 \text{ cm}^{-1}$ , accounting for the width of absorption bands (Balan et al. 2008). Theoretical absorption coefficients were then obtained from the low-frequency dielectric permittivity tensor using the approach detailed in the Appendix.

## Results and discussion

The enstatite structure displays two types of octahedral sites nominally occupied by Mg<sup>2+</sup> cations. The Mg<sup>2+</sup> cations at the M1 site are bound to four O1 and two O2 oxygen atoms, corresponding to apical and equatorial non-bridging oxygen in silicate tetrahedra, respectively. The more distorted M2 sites involve O1 and O2 oxygen atoms and the silicate-bridging O3 oxygen atoms. Previous theoretical

studies consistently indicate that the protonation of vacant M2 sites is significantly favored with respect to that of M1 sites (Gatzemeier and Wright 2006; Balan et al. 2013; Xue et al. 2024). In the fully protonated M2 vacancies, the two non-equivalent O2–H groups (referred to as OaH and ObH) are oriented in the (100) plane, leading to two bands dominantly polarized along the [001] direction. The shorter ObH bond vibrates at ~ 3360 cm<sup>-1</sup> and the other OaH bond at ~ 3070 cm<sup>-1</sup> (e.g., Rauch and Keppler 2002; Stalder and Skogby 2002; Stalder 2004). The theoretical frequencies obtained in the present modelling are 3425 and 3134 cm<sup>-1</sup> (Table 1). Differences with the theoretical frequencies previously obtained with the PBE functional by Balan et al. (2013) (3361 and 3034 cm<sup>-1</sup>) and Xue et al. (2024) (3361 and 3161 cm<sup>-1</sup>) are mostly due to the use of different sets of pseudopotentials and different size of supercells.

Based on their polarization properties, the bands observed by Stalder (2004) in the doped enstatite samples can be assumed to be related to M vacancies. Accordingly, a series of models was built by removing one proton from the previously investigated protonated M2 vacancy and introducing trivalent cations (Al, Cr, Fe) in the neighboring M1 sites (Table 1). The association of one proton and one trivalent impurity compensates for the charge deficit due to the Mg vacancy and ensures the electrostatic neutrality of the defect. In each model, a single M<sup>3+</sup> for Mg<sup>2+</sup> substitution

was considered and it was assumed that the OH group is not coordinated to the trivalent cation due to the bond valence constraints. Each composition thus leads to four defect configurations (Fig. 2). In configurations 1 and 2, the hydrogen is bonded to the Ob oxygen, while it is bonded to Oa in configurations 3 and 4. The substitution affects the octahedral site almost facing the OH group along the [001] direction in configurations 1 and 4, and the site in a more lateral position in configurations 2 and 3. Only substitutions at M1 sites were considered for the Cr and Fe-bearing systems, but two additional defect models were considered in the aluminous system to account for potential Al for Si substitution affecting the two non-equivalent Si sites of enstatite (Table 1).

The presence of neighboring impurities has a significant effect on the vibrational properties of the OH group at the vacant M2 site (Table 1). As is usually observed, the stretching frequency is inversely correlated with the OH bond length (Fig. 3A). The slope of the correlation (~ - 19,000 cm<sup>-1</sup>/Å) is similar to that previously reported for hydrous defects in enstatite and other minerals (e.g., Balan et al. 2013, 2020). For the OH defects associated with M2 vacancies, the OH bond length appears to be mostly controlled by the strength of H-bonding, as attested by its regular decrease as a function of the oxygen-oxygen distance (Fig. 3B). Compared with the fully protonated vacancy, the presence of a trivalent cation in the coordination sphere of

**Table 1** Theoretical properties of OH-defects in enstatite (structure files are provided in the Supplement)

Model	Protonated oxygen	rel. energy* (kJ/mol)	rel. abundance at 1500 K (%)**	d <sub>OH</sub> (Å)	d <sub>O(H)...O</sub> (Å)	ω <sub>OH</sub> (cm <sup>-1</sup> )	I <sub>x</sub> *** (%)	I <sub>y</sub> *** (%)	I <sub>z</sub> *** (%)	K <sub>int</sub> (cm <sup>-2</sup> per molH <sub>2</sub> O/L)	ω <sub>exp</sub> **** (cm <sup>-1</sup> )	
1	[(1H <sup>+</sup> ) <sub>M2</sub> (Al <sup>3+</sup> ) <sub>M1</sub> ] <sup>x</sup> _1	O2b	7.3	23.5	0.9776	3.1797	3584	17	8	75	72,000	3548
2	[(1H <sup>+</sup> ) <sub>M2</sub> (Al <sup>3+</sup> ) <sub>M1</sub> ] <sup>x</sup> _2	O2b	12.4	15.6	0.9784	3.0836	3563	3	19	78	89,000	3475
3	[(1H <sup>+</sup> ) <sub>M2</sub> (Al <sup>3+</sup> ) <sub>M1</sub> ] <sup>x</sup> _3	O2a	10.1	18.8	0.9880	2.8649	3373	3	34	63	159,000	3320
4	[(1H <sup>+</sup> ) <sub>M2</sub> (Al <sup>3+</sup> ) <sub>M1</sub> ] <sup>x</sup> _4	O2a	0	42.2	0.9836	2.9820	3474	14	23	63	94,000	3381
5	[(1H <sup>+</sup> ) <sub>M2</sub> (Fe <sup>3+</sup> ) <sub>M1</sub> ] <sup>x</sup> _1	O2b	2.0	42.6	0.9784	3.0800	3558	7	11	82	105,000	3461
6	[(1H <sup>+</sup> ) <sub>M2</sub> (Fe <sup>3+</sup> ) <sub>M1</sub> ] <sup>x</sup> _2	O2b	34.2	3.2	0.9792	3.0575	3545	5	26	69	101,000	n.o.
7	[(1H <sup>+</sup> ) <sub>M2</sub> (Fe <sup>3+</sup> ) <sub>M1</sub> ] <sup>x</sup> _3	O2a	31.8	3.9	0.9908	2.8265	3313	4	43	53	188,000	n.o.
8	[(1H <sup>+</sup> ) <sub>M2</sub> (Fe <sup>3+</sup> ) <sub>M1</sub> ] <sup>x</sup> _4	O2a	0	50.2	0.9875	2.8661	3379	6	21	73	167,000	3328
9	[(1H <sup>+</sup> ) <sub>M2</sub> (Cr <sup>3+</sup> ) <sub>M1</sub> ] <sup>x</sup> _1	O2b	7.4	23.3	0.9793	3.0801	3547	7	13	80	106,000	3449
10	[(1H <sup>+</sup> ) <sub>M2</sub> (Cr <sup>3+</sup> ) <sub>M1</sub> ] <sup>x</sup> _2	O2b	12.5	15.5	0.9796	3.0531	3538	4	25	71	100,000	3449
11	[(1H <sup>+</sup> ) <sub>M2</sub> (Cr <sup>3+</sup> ) <sub>M1</sub> ] <sup>x</sup> _3	O2a	9.8	19.2	0.9903	2.8329	3326	3	41	56	185,000	3283
12	[(1H <sup>+</sup> ) <sub>M2</sub> (Cr <sup>3+</sup> ) <sub>M1</sub> ] <sup>x</sup> _4	O2a	0	42.1	0.9876	2.8867	3386	7	23	70	157,000	3322
13	(Al <sup>3+</sup> ,H <sup>+</sup> ) <sub>Si</sub> <sup>x</sup> _1	O2a	21	15.5	0.9732	2.9091	3602	37	56	7	68,000	n.o.
14	(Al <sup>3+</sup> ,H <sup>+</sup> ) <sub>Si</sub> <sup>x</sup> _2	O2b	0	84.5	0.9837	2.9464	3430	52	10	38	104,000	n.o.
15	(2H <sup>+</sup> ) <sub>M2</sub>	O2a			0.9994	2.7890	3134	0	33	67	260,000	3070
		O2b			0.9845	3.0035	3425	0	25	75	163,000	3361

n.o. not observed

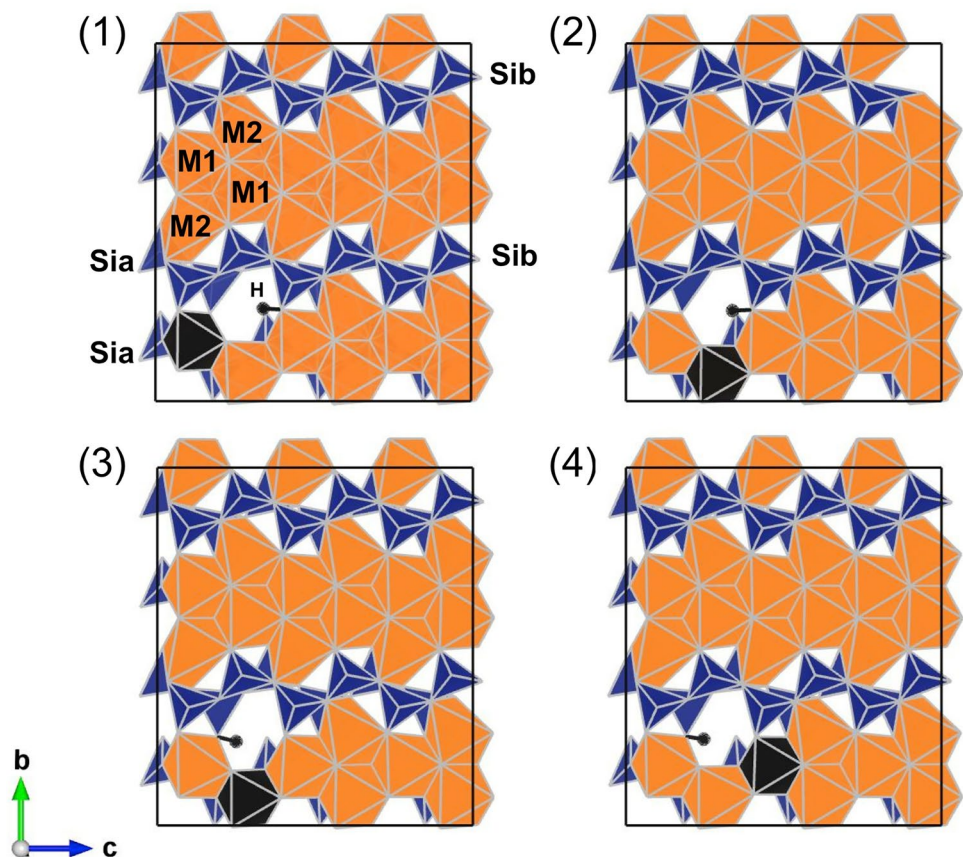
\*The relative energy is defined with respect to the most stable configuration of the model with the same stoichiometry

\*\*The relative abundances are obtained using a Boltzmann distribution at 1500 K applied to the models with the same stoichiometry

\*\*\*I<sub>x</sub>, I<sub>y</sub>, I<sub>z</sub> correspond to the relative intensities for polarizations parallel to [100], [010] and [001], respectively

\*\*\*\*Stalder (2004)

**Fig. 2** Configurations of OH-bearing defects associated to M2 vacancies and  $M^{3+}$  substitution at M1 site. View along the [100] direction of the  $1 \times 2 \times 3$  supercell. Tetrahedral Si site: blue, octahedral Mg sites: orange, H atom: black sphere. The substituted octahedral M1 site is in black. Configurations (1) and (2) correspond to protonation of O2b. Configurations (3) and (4) correspond to protonation of O2a. In configurations (1) and (4) the substituted site faces the OH group, while it is in a more lateral position in configurations (2) and (3)



the H-bond accepting oxygen contributes to the local charge compensation, leading to a weakening of the H-bond and a shortening of the OH bond. The relation of the theoretical harmonic OH stretching frequency as a function of oxygen–oxygen distance is consistent with its experimental counterpart (Libowitzky 1999) when the experimentally observed frequencies are corrected for anharmonicity (Fig. 3C, see the appendix for the estimation of the effect of anharmonicity on frequency). The inverse linear correlation of the absorption coefficient with the stretching frequency (Fig. 3D) is similar to that inferred from the theoretical modeling of OH groups in minerals (Balan et al. 2008). Its slope is consistent with that inferred from experimental data (e.g., Libowitzky and Rossman 1997; Stalder et al. 2012) when the experimental frequencies are corrected for anharmonicity (Fig. 3D).

For each chemical composition, significant differences in the relative energy and OH stretching frequency are observed between the various configurations of the defects. At equivalent positions of the trivalent cation in M1, the configurations 3 and 4, corresponding to the protonation of Oa, are more stable and lead to lower stretching frequencies than those which involve Ob, configurations 2 and 1, respectively. The position of the substituted site has a significant influence too. In models 1 and 4, the electrostatic charge

excess at the substituted site can increase the stretching frequency of the facing OH group by several dozens of  $\text{cm}^{-1}$  with respect to the model in which the substituted site is in a more lateral position with respect to the OH group (models 2 and 3, respectively). The facing configurations (1 and 4) are also energetically favored with respect to the lateral ones.

For the Fe-bearing models (Table 1), the energy difference between the configurations can be particularly important ( $> 30 \text{ kJ/mol}$ ). The relative abundance of the two less stable configurations (2 and 3) is not expected to exceed a few percent at 1500 K (1227 °C), while that of the two other configurations is above 40% (Table 1). Consistently, the Fe-bearing samples synthesized by slow cooling from 1400 to 1150 °C only display two specific bands at  $3461 \text{ cm}^{-1}$  and  $3328 \text{ cm}^{-1}$  (Stalder 2004). These two bands can thus be confidently assigned to the two more stable geometries of the Fe-bearing models, i.e., configurations 1 and 4, respectively (Table 1).

For the Cr-bearing models, the energy difference between the four configurations is smaller and all four configurations are expected to occur in the synthetic Cr-bearing samples (Table 1). The configuration 4 is expected to be dominant (42% at 1500 K), while the relative abundances of the three other configurations range between 15 and 25%. Based on their relative intensities (Fig. 1) and stretching frequencies

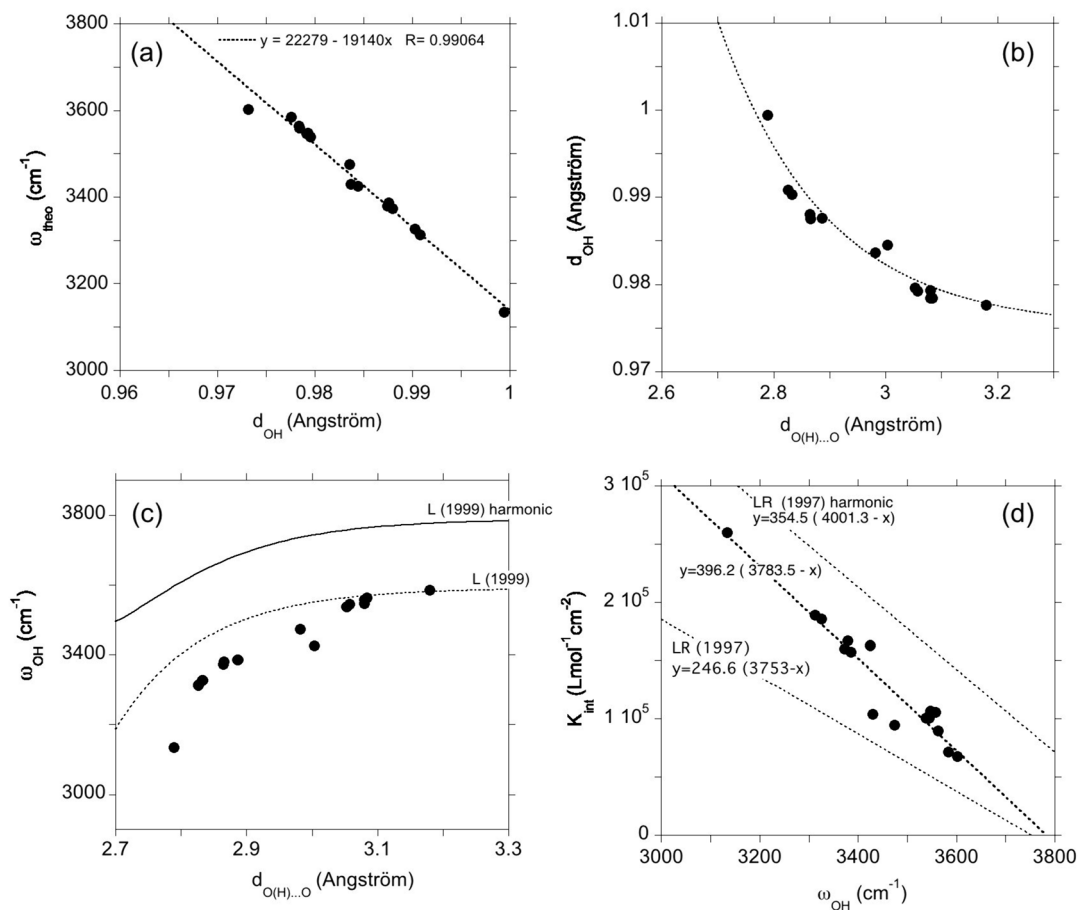


**Fig. 3** **a** Relation between the theoretical stretching frequency and OH bond length for the investigated defects. **b** Relation between the OH bond length and the oxygen-oxygen distance describing the hydrogen bond in protonated M2 vacancies. The dotted line is a guide for the eye. **c** Relation between the harmonic OH stretching frequency and the OH bond length in protonated M2 vacancies. The dotted line corresponds to the experimental relation of Libowitzky (1999)

and the solid line is the same relation corrected for anharmonicity (Appendix B). **d** Theoretical integrated molar absorption coefficients of the stretching modes of OH defects as a function of the stretching frequency. The bottom line corresponds to the calibration of Libowitzky and Rossman (1997). When corrected for anharmonicity (top line; Appendix B), the slope of the experimental calibration is closer to the theoretical slope

(Table 1), the bands experimentally observed at 3283 and 3322 cm<sup>-1</sup> (Stalder 2004) can be assigned to configurations 3 and 4, respectively. Considering that the theoretical stretching frequencies of the two other configurations are close to each other, it is possible that these two configurations contribute to the remaining band at 3449 cm<sup>-1</sup>. This would explain its comparatively strong absorbance, similar to that of the band at 3322 cm<sup>-1</sup>, which is assigned to the more stable configuration 4. Alternatively, it cannot be fully excluded that the energy difference between the configurations 1 and 2 is larger than theoretically expected (Table 1) and that only the most stable of the two configurations is actually observed.

The relative stabilities of the Al-bearing models are similar to those computed for the Cr-bearing defects (Table 1). On the same criteria as for the Cr-bearing samples, the two bands observed at 3320 and 3381 cm<sup>-1</sup> are assigned to

configurations 3 and 4, respectively. The two major bands at 3475 and 3548 cm<sup>-1</sup> observed in the Al-doped sample with the lowest Al concentrations (Stalder and Skogby 2002; Stalder 2004) are assigned to the two remaining configurations (configurations 2 and 1, respectively) (Table 1). A minor band at 3517 cm<sup>-1</sup> is also observed in the spectrum of the Al-0.25 sample with a polarization similar to that of the other bands assigned to M2 vacancies (Fig. 1). This minor band becomes dominant in the Al-rich samples (Stalder 2004) which suggests that it could be related to a medium-range environment of M2 vacancies involving more than a single Al atom. A comparatively more complex speciation of OH groups could thus occur in Al-bearing samples depending on their synthesis conditions (see also Rauch and Keppler 2002).

In the models with tetrahedral Al, the underbonded O2 atom is the most favorable site for the proton location due

to bond valence requirements, as in diopside (Balan et al. 2020). The defect involving the larger Sib site is significantly favored ( $> 20$  kJ/mol) with respect to that involving the smaller Sia site (Table 1). The Sia and Sib models display different OH bond lengths leading to theoretical OH stretching frequencies of 3602 and 3430  $\text{cm}^{-1}$ , respectively, with dominant polarizations along [010] and [100], respectively (Table 1). The polarization properties of OH bands associated to tetrahedral substitutions thus markedly differ from those associated to M2 vacancies. It is noteworthy that Grant et al. (2007) report two bands with a different polarization at 3600 and 3390  $\text{cm}^{-1}$  in synthetic enstatite with higher Al concentrations. Unfortunately, it was not possible to unambiguously relate these bands to simple models of OH-bearing defects. Even though the stretching frequencies reported by Grant et al. (2007) are close to those obtained for the models with tetrahedral Al (Table 1), the relative intensities of the experimental bands are more difficult to reconcile with the theoretical expectations.

A plot of the theoretical (harmonic) OH stretching frequencies versus experimentally observed (anharmonic) frequencies of the OH bands in enstatite summarizes the results in Fig. 4. They show a linear trend similar to the one previously observed for diopside, with a positive offset of theoretical frequencies around 50–70  $\text{cm}^{-1}$  (Balan et al. 2020). This modest offset is consistent with the opposite effects of the neglect of anharmonicity and the use of the

PBE functional in the calculation of theoretical frequencies (Balan et al. 2007).

## Conclusions

Isolated defects involving a coupled incorporation of trivalent cation and proton in enstatite can be theoretically investigated using periodic models based on large super-cells. This facilitates the comparison of the theoretical results with observations made on samples with low levels of doping and low hydrogen content. In this case, it is possible to unambiguously assign most of the experimentally observed bands to specific defect configurations. These bands correspond to neutral defects corresponding to protonated M2 vacancies associated with a trivalent cation substitution at a neighboring M1 site. The theoretical modeling thus confirms that the  $\text{M}^{3+} + \text{H}^+ = 2 \text{Mg}^{2+}$  exchange mechanism is the dominant hydrogen incorporation mechanism at the lowest concentration levels in enstatite doped with trivalent cations (Stalder and Skogby 2002; Stalder 2004). For the Fe- and Al-bearing enstatite, the appearance of additional bands and the significant broadening of the bands observed when the trivalent cation and hydrogen contents increase (Stalder 2004) suggests that more complex incorporation mechanisms occur. These changes potentially involve substitutions affecting tetrahedral sites and more significant electrostatic or elastic interactions between the defects at elevated concentrations. Their modeling will require different strategies accounting for these interactions and for the multiplicity of potential configurations.

## Appendix

### Computation of theoretical absorption coefficients

Considering the propagation of an IR beam through a section of an isotropic medium, the integrated absorbance is defined by:

$$A = \int_{\bar{\nu}} \log_{10} \left( \frac{I_0}{I_t} \right) d\bar{\nu} = \frac{1}{\ln(10)} \int_{\bar{\nu}} \ln \left( \frac{I_0}{I_t} \right) d\bar{\nu} \quad (1)$$

where  $\bar{\nu}$  is the frequency in wavenumbers and  $I_0$  and  $I_t$  are the intensity of the incident and transmitted light, respectively.

Let  $n = n_1 + i n_2$  be the (frequency dependent) complex refractive index of the medium, the absorbance is related to the imaginary part of the refractive index  $n_2$  by (Bruesch 1986):

$$\ln \left( \frac{I_0}{I_t} \right) = 4\pi\bar{\nu}n_2 \quad (2)$$

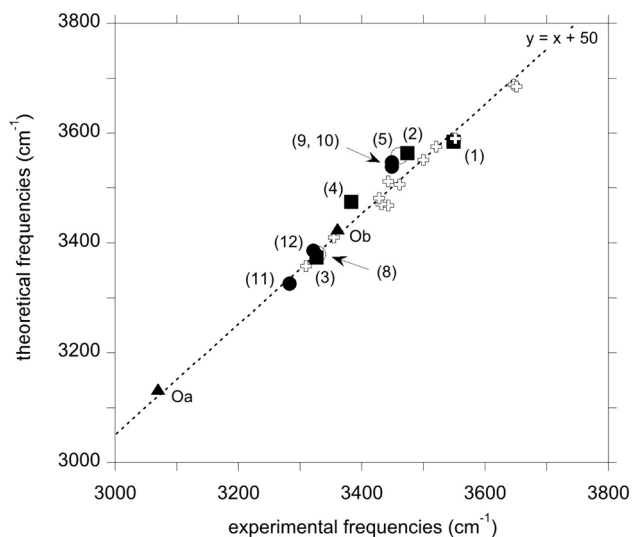


**Fig. 4** Comparison of theoretical and observed OH stretching frequencies for the relevant defect models. The labels refer to Table 1. Triangles: doubly protonated M2 vacancy (contribution from protonation of Oa and Ob oxygens is indicated), squares: Al-bearing defects, open circles: Fe-bearing defects, full circles: Cr-bearing defects, open crosses: OH-bearing defects in diopside (Balan et al. 2020)

The imaginary part of the refractive index is related to the complex (frequency dependent) dielectric function by:

$$2n_2^2 = (\epsilon_1^2 + \epsilon_2^2)^{1/2} - \epsilon_1 \tag{3}$$

where  $\epsilon_1$  and  $\epsilon_2$  are its real and imaginary parts, respectively. Considering that  $\epsilon_2 = 2 n_1 n_2$ , Eq. (2) is equivalently expressed as:

$$\ln\left(\frac{I_0}{I_t}\right) = 2\pi\bar{\nu}\frac{\epsilon_2}{n_1} \tag{4}$$

For a dilute species in a non-absorbing medium, the Beer-Lambert law (e.g., Mayerhöfer and Popp 2019) relates the integrated absorbance to the molar concentration  $C$  of the absorbing species:

$$A = K C t \tag{5}$$

where  $K$  is the absorption coefficient and  $t$  the thickness of the sample. When the species of interest is a molecular impurity in a crystal, such as an OH group, it is appropriate to use the total absorbance  $A_{tot}$  which is the sum of absorbances normalized to thickness in all three orthogonal polarization directions (Libowitzky and Rossman 1996, 1997). The total integrated absorption coefficient  $K_{int}$  can thus be defined as:

$$A_{tot} = K_{int} C \tag{6}$$

For an isotropic crystal,  $K_{int}$  is three times as large as  $K$ , which is defined for a single direction. For crystals with orthorhombic symmetry or higher, the principal axes of the refraction and dielectric tensors are determined by the symmetry (Sambridge et al. 2008) and  $K_{int}$  can be determined using Eqs. (1), (2) and (3) for each polarization.

It is noteworthy that quantum chemistry codes often provide the infrared absorptivities  $I_k$  of vibrational mode  $k$  in  $(D/\text{\AA})^2/\text{amu}$ , which can be converted to an integrated absorption coefficient. For a non-degenerate mode, the relation of  $I_k$  to the absorption coefficient  $K$  (in  $\text{km/mol}$ ) of a molecular species in gas phase is (e.g., Monguzzi et al. 2009):

$$K = I_k \times 42.256 / \ln(10) \tag{7}$$

In this case,  $n_1$  in Eq. (4) is approximately equal to one. For a weakly absorbing molecular impurity diluted in a condensed phase,  $n_1$  usually differs from one but it can be assumed to be constant and close to the refractive index of the host medium. The theoretical absorptivities of OH stretching modes in  $(D/\text{\AA})^2/\text{amu}$  is then related to the integrated absorption coefficients  $K_{int}$  in  $\text{cm}^{-2}$  per  $\text{mol}(\text{H}_2\text{O}) \cdot \text{L}^{-1}$  by:

$$K_{int} \approx I_k \times 4225.6 \times 3 \times 2 / (n_{host} \times \ln(10)) \tag{8}$$

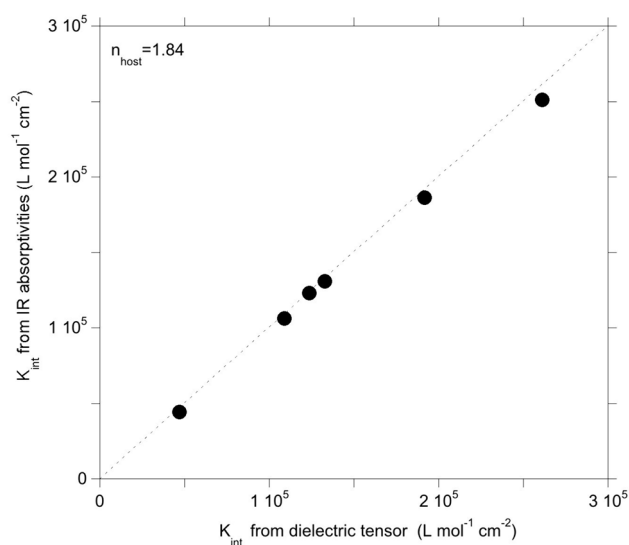


**Fig. 5** Comparison of absorption coefficients obtained from the theoretical dielectric tensor components with those obtained from theoretical IR absorptivities (Eq. 8) for a series of OH defects in corundum previously investigated by Balan (2020) and Jollands and Balan (2022)

where  $n_{host}$  is the average refractive index of the host. The factor 2 in Eq. (8) is related to the use of  $\text{H}_2\text{O}$  equivalent and the factor 3 accounts for the use of total intensities, instead of considering a single direction as in the definition of  $K$  (Wilson et al. 1980). Benchmarking calculations performed on a series of OH bearing defects in corundum previously investigated by Balan (2020) and Jollands and Balan (2022) indicate that the two different approaches provide absorption coefficients differing by less than a few percent (Fig. 5).

### Effect of OH bond anharmonicity on the IR absorption calibration curves

The anharmonic shift ( $2\omega_e x_e$ ) related to the anharmonicity of the OH potential increases when the stretching frequency decreases (Wöhlecke and Kovács 2001). An approximate polynomial relation (Fig. 6) between the anharmonicity constant and the observed (anharmonic) stretching frequency can be obtained using the experimental data on solid hydrates reported by Berglund et al. (1978). By combining this relation with the correlation reported by Libowitzky and Rossmann (1997), an experimental relation between the absorption coefficient and the harmonic stretching frequency can be obtained:

$$K_{int} = 354.5 (4001.3 - \omega_{OH})$$

where  $K_{int}$  is the integrated absorption coefficients in  $\text{cm}^{-2}$  per  $\text{mol}(\text{H}_2\text{O}) \cdot \text{L}^{-1}$  and  $\omega_{OH}$  is the harmonic stretching

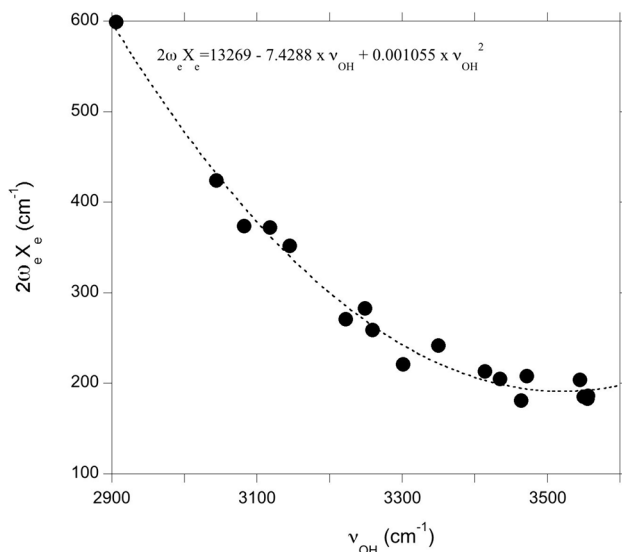


**Fig. 6** Experimental relation between the anharmonicity parameter and the OH stretching frequency from the Table 1 of Berglund et al. (1978). The value for free hydroxyl (Wöhlecke and Kovács 2001) has also been included. The dotted line corresponds to a quadratic polynomial interpolation which can be used to assess the harmonic stretching frequencies from experimentally observed frequencies

frequency. In this case, the theoretical slope is significantly closer to the experimental one (Fig. 3d). The anharmonicity correction also improves the comparison of the theoretical and experimental relations between the OH stretching frequency and the oxygen–oxygen distance (Fig. 3c). This supports the idea that the apparent discrepancies between theoretical and experimental correlations are mostly related to the assumptions made in the calculation of theoretical frequencies.

**Supplementary Information** The online version contains supplementary material available at <https://doi.org/10.1007/s00269-024-01289-2>.

**Acknowledgements** We thank Roland Stalder and two anonymous reviewers for their constructive comments. Calculations were performed using the HPC resources of the SACADO MeSU platform at Sorbonne Université and the HPC resources of IDRIS under allocation 2022-AD010910820R1 attributed by GENCI (Grand Équipement National de Calcul Intensif).

**Author contributions** JI and EB designed the study. EB performed the simulations. All co-authors discussed the results and prepared the manuscript.

**Data and code availability** Structure drawings have been produced with the Vesta software (Momma and Izumi 2011). PWscf and PHonon codes (Giannozzi et al. 2009) are available at <http://www.quantum-espresso.org>. Model structures are provided as electronic supplementary files under “.cif” formats.

## References

- Balan E (2020) Theoretical infrared spectra of OH defects in corundum ( $\alpha$ -Al<sub>2</sub>O<sub>3</sub>). *Eur J Mineral* 32:457–467. <https://doi.org/10.5194/ejm-32-457-2020>
- Balan E, Lazzeri M, Delattre S, Meheut M, Refson K, Winkler B (2007) Anharmonicity of inner-OH stretching modes in hydrous phyllosilicates: assessment from first-principles frozen-phonon calculations. *Phys Chem Minerals* 34:621–625. <https://doi.org/10.1007/s00269-007-0176-4>
- Balan E, Refson K, Blanchard M, Delattre S, Lazzeri M, Ingrin J, Mauri F, Wright K, Winkler B (2008) Theoretical infrared absorption coefficient of OH groups in minerals. *Am Mineral* 93:950–953. <https://doi.org/10.2138/am.2008.2889>
- Balan E, Blanchard M, Yi H, Ingrin J (2013) Theoretical study of OH-defects in pure enstatite. *Phys Chem Minerals* 40:41–50. <https://doi.org/10.1007/s00269-012-0544-6>
- Balan E, Paulatto L, Liu J, Ingrin J (2020) Low-temperature infrared spectrum and atomic-scale structure of hydrous defects in diopside. *Eur J Mineral* 32:505–520. <https://doi.org/10.5194/ejm-32-505-2020>
- Baroni S, de Gironcoli S, Dal Corso A, Giannozzi P (2001) Phonons and related crystal properties from density-functional perturbation theory. *Rev Mod Phys* 73:515–561. <https://doi.org/10.1103/RevModPhys.73.515>
- Beran A, Zemann J (1986) The pleochroism of a gem-quality enstatite in the region of the OH stretching frequency, with a stereochemical interpretation. *Tschermaks Mineral Petrog Mitt* 35:19–25
- Berglund B, Lindgren J, Tegenfeldt J (1978) O-H and O-D stretching vibrations in isotopically dilute HDO molecules in some solid hydrates. *J Mol Struct* 43:169–177
- Bruesch P (1986) Phonons theory and experiments II: experiments and interpretation of experimental results. *Solid-State Sciences* 65, Springer Series, Berlin
- Fuchs Y, Fourdrin C, Balan E (2022) Theoretical OH-stretching vibrations in dravite. *Eur J Mineral* 34:239–251. <https://doi.org/10.5194/ejm-34-239-2022>
- Gatzemeier A, Wright K (2006) Computer modelling of hydrogen defects in the clinopyroxenes diopside and jadeite. *Phys Chem Minerals* 33:115–125. <https://doi.org/10.1007/s00269-006-0059-0>
- Giannozzi P, Baroni S, Bonini N et al (2009) Quantum ESPRESSO: a modular and open-source software project for quantum simulations of materials. *J Phys: Cond Mat* 21:395502. <https://doi.org/10.1088/0953-8984/21/39/395502>
- Grant KJ, Kohn SC, Brooker RA (2007) Solubility and partitioning of water in synthetic forsterite and enstatite in the system MgO–SiO<sub>2</sub>–H<sub>2</sub>O±Al<sub>2</sub>O<sub>3</sub>. *Contrib Mineral Petrol* 151:651–664. <https://doi.org/10.1007/s00410-006-0082-7>
- Hamann DR (2013) Optimized norm-conserving Vanderbilt pseudopotentials. *Phys Rev B* 88:085117. <https://doi.org/10.1103/PhysRevB.88.085117>
- Ingrin J, Skogby H (2000) Hydrogen in nominally anhydrous upper-mantle minerals: concentration levels and implications. *Eur J Mineral* 12:543–570. <https://doi.org/10.1127/ejm/12/3/0543>
- Jollands MC, Balan E (2022) Beryllium incorporation in corundum. *Mineral Mag* 86:758–766. <https://doi.org/10.1180/mgm.2022.63>
- Libowitzky E (1999) Correlation of OH stretching frequencies and O–H...O hydrogen bond length in minerals. *Monat Chem* 130:1047–1059. <https://doi.org/10.1007/BF03354882>
- Libowitzky E, Rossman GR (1996) Principles of quantitative absorbance measurements in anisotropic crystals. *Phys Chem Minerals* 23:319–327. <https://doi.org/10.1007/BF00199497>
- Libowitzky E, Rossman GR (1997) An IR absorption calibration for water in minerals. *Am Mineral* 82:1111–1115. <https://doi.org/10.2138/am-1997-11-1208>



- Mayerhöfer TG, Popp J (2019) Beer's law derived from electromagnetic theory. *Spectrochim Acta Part A Mol Biomol Spectrosc* 215:345–347. <https://doi.org/10.1016/j.saa.2019.02.103>
- Mierdel K, Keppler H (2004) The temperature dependence of water solubility in enstatite. *Contrib Mineral Petrol* 148:305–311. <https://doi.org/10.1007/s00410-004-0605-z>
- Momma K, Izumi F (2011) VESTA 3 for three-dimensional visualization of crystal, volumetric and morphology data. *J Appl Crystallogr* 44:1272–1276. <https://doi.org/10.1107/S0021889811038970>
- Monguzzi A, Milani A, Lodi L, Trioni M, Tubino R, Castiglioni C (2009) Vibrational overtones quenching of near infrared emission in  $\text{Er}^{3+}$  complexes. *New J Chem* 33:1542–1548. <https://doi.org/10.1039/b901272a>
- Morimoto N, Koto K (1969) The crystal structure of orthoenstatite. *Zeit Kristallo* 129:65–83
- Perdew JP, Burke K, Ernzerhof M (1996) Generalized gradient approximation made simple. *Phys Rev Lett* 77:3865–3868. <https://doi.org/10.1103/PhysRevLett.77.3865>
- Prechtel F, Stalder R (2010) FTIR spectroscopy with a focal plane array detector: a novel tool to monitor the spatial OH-defect distribution in single crystals applied to synthetic enstatite. *Am Mineral* 95:888–891. <https://doi.org/10.2138/am.2010.3497>
- Prechtel F, Stalder R (2011) The potential use of OH-defects in enstatite as geobarometer. *Contrib Mineral Petrol* 162:615–623. <https://doi.org/10.1007/s00410-011-0615-6>
- Rauch M, Keppler H (2002) Water solubility in orthopyroxene. *Contrib Mineral Petrol* 14:525–536. <https://doi.org/10.1007/s00410-002-0365-6>
- Sambridge M, Gerald JF, Kovacs I, O'Neill HSC, Hermann J (2008) Quantitative absorbance spectroscopy with unpolarized light: part I physical and mathematical development. *Am Mineral* 93:751–764. <https://doi.org/10.2138/am.2008.2657>
- Schlipf M, Gygi F (2015) Optimization algorithm for the generation of ONCV pseudopotentials. *Comput Phys Comm* 196:36. <https://doi.org/10.1016/j.cpc.2015.05.011>
- Stalder R (2004) Influence of Fe, Cr and Al on hydrogen incorporation in orthopyroxene. *Eur J Mineral* 16:703–711. <https://doi.org/10.1127/0935-1221/2004/0016-0703>
- Stalder R, Skogby H (2002) Hydrogen incorporation in enstatite. *Eur J Mineral* 14:1139–1144. <https://doi.org/10.1127/0935-1221/2002/0014-1139>
- Stalder R, Prechtel F, Ludwig T (2012) No site-specific infrared absorption coefficient for OH-defects in pure enstatite. *Eur J Mineral* 24:465–470. <https://doi.org/10.1127/0935-1221/2012/0024-2180>
- Stalder R, Karimova A, Konzett J (2015) OH-defects in multiple-doped orthoenstatite at 4–8 GPa: filling the gap between pure and natural systems. *Contrib Mineral Petrol* 169:38. <https://doi.org/10.1007/s00410-015-1133-8>
- Wilson EB, Decius JC, Cross PC (1980) *Molecular vibrations: the theory of infrared and raman vibrational spectra*. Dover Publications, New York
- Wöhlecke M, Kovács L (2001) OH<sup>-</sup> ions in oxide crystal. *Crit Rev S State Mater Sci* 25:1–86. <https://doi.org/10.1080/20014091104161>
- Xue X, Kanzaki M, Djirar AE, Gregson C (2024) Incorporation mechanisms and infrared absorption coefficients of water in  $\text{MgSiO}_3$  orthoenstatite clarified via comprehensive NMR and vibrational spectroscopic measurements, and first-principles calculations. *Contrib Mineral Petrol* 179:33. <https://doi.org/10.1007/s00410-024-02114-3>

**Publisher's Note** Springer Nature remains neutral with regard to jurisdictional claims in published maps and institutional affiliations.

Springer Nature or its licensor (e.g. a society or other partner) holds exclusive rights to this article under a publishing agreement with the author(s) or other rightsholder(s); author self-archiving of the accepted manuscript version of this article is solely governed by the terms of such publishing agreement and applicable law.